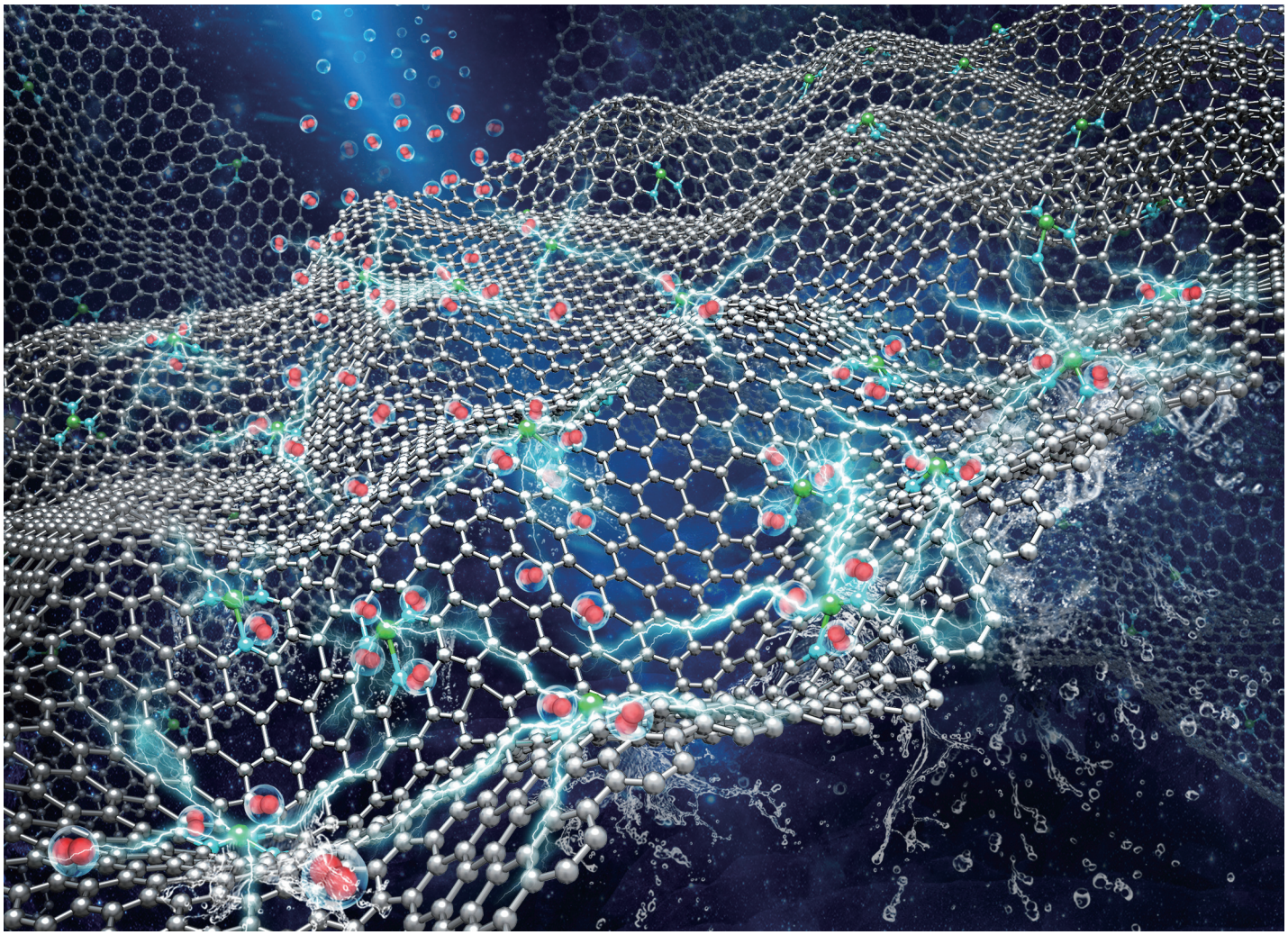

Highlighting results from the Chen group in the University of California – Santa Cruz and the Zou lab in American University.

Ordered mesoporous carbons codoped with nitrogen and iron as effective catalysts for oxygen reduction reaction

Controlled pyrolysis of poly(o-phenylenediamine) films grown on silica colloid surfaces (along with melamine and iron chloride) leads to the formation of highly ordered mesoporous carbons co-doped with nitrogen and iron after the removal of the colloidal templates. The obtained carbons exhibit apparent electrocatalytic activity for the reduction of oxygen to water in alkaline media, which is primarily ascribed to nitrogen dopants, with minimal contributions from the iron species.

As featured in:

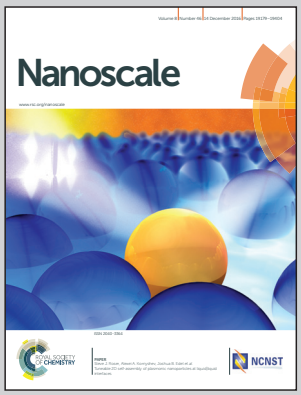

See Shouzhong Zou, Shaowei Chen *et al.*, *Nanoscale*, 2016, **8**, 19249.

ROYAL SOCIETY OF CHEMISTRY

www.rsc.org/nanoscale

Registered charity number: 207890

Nanoscale

PAPER

View Article Online
View Journal | View Issue

Cite this: *Nanoscale*, 2016, **8**, 19249

Ordered mesoporous carbons codoped with nitrogen and iron as effective catalysts for oxygen reduction reaction†

Xiaojun Liu,[a] Shouzhong Zou*[a] and Shaowei Chen*[b]

Doping with foreign atoms is an effective approach to significantly enhance the catalytic performance of carbon materials for oxygen reduction reaction (ORR). In this paper, a colloidal silica template method was employed to synthesize nitrogen and iron codoped ordered mesoporous carbon for ORR electrocatalysis. The carbon materials were thoroughly characterized by transmission electron microscopy, Raman spectroscopy, X-ray diffraction, and X-ray photoelectron spectroscopy measurements. The porosity was quantified by nitrogen adsorption/desorption measurements that showed the formation of ordered mesoporous structures with a BET specific surface area up to 953.8 m^2 g^{-1} and the mesopores mostly centered at *ca.* 25 nm, close to the size of the colloidal silica. The resulting mesoporous carbon exhibited apparent ORR activity in alkaline media, which was highly comparable to that of commercial Pt/C (20 wt%), with the onset potential at +0.99 V *vs.* RHE. This was ascribed largely to nitrogen dopants, with additional contributions from the trace amounts of iron dopants, and the reactions appeared to be facilitated by the formation of a mesoporous structure. Moreover, the mesoporous carbon showed better stability, resistance against fuel crossover, and selective activity than Pt/C. This work demonstrates a new paradigm for the preparation of heteroatom-doped carbon materials that are promising alternatives to Pt-based catalysts for fuel cells.

Received 26th July 2016,
Accepted 3rd October 2016

DOI: 10.1039/c6nr05884a

www.rsc.org/nanoscale

Introduction

In fuel cell electrocatalysis, Pt and Pt-based alloys have been regarded as the most efficient catalysts for fuel oxidation at the anode and ORR at the cathode; yet the prohibitive costs and scarcity of Pt significantly hinder their large-scale commercial applications.[1] The poor durability of Pt also limits the long-term operation. To mitigate these issues, great efforts have been devoted to develop inexpensive, durable, high-performance alternatives to Pt-based ORR electrocatalysts. Among these, nitrogen-doped carbons have been recognized as a viable ORR catalyst, as manifested with nitrogen-doped carbon nanotube arrays that exhibited high ORR activity.[2] Thus far, a wide range of carbon materials has been used, including carbon nanotubes,[3,4] graphene[5–7] and porous carbon,[8–12] where the embedded nitrogen atoms can modify the local electron density of neighboring carbon atoms and facilitate oxygen adsorption and dissociation.[4,13,14] Moreover, addition of transition metals such as Fe and Co[15–20] to N-doped carbon can further improve the electrocatalytic performance, as the transition metals may either serve as part of the ORR active sites or assist the formation of the active sites.[21–23] Therefore, the selection of appropriate precursors to prepare the catalysts is a critical first step. An ideal precursor should provide abundant C and N sources, and even metal elements. Some progress has been made along this direction. For instance, iron(II) phthalocyanine,[24] vitamin B12,[16] and ionic liquids[25,26] have been used as precursors to prepare carbon-based catalysts doped with heteroatoms.

Additionally, it is generally desired to have a large surface area, appropriate mesoporosity and high electrochemical stability of the ORR catalysts, in order to expose a maximal number of accessible active sites as well as to facilitate mass transport of reaction species within the catalysts. For instance, He *et al.* prepared hierarchically porous N-doped carbon using polydopamine-modified mixed cellulose ester filter films as the sole template and KOH as the activating reagent.[27] We synthesized highly ordered hierarchical mesoporous carbon by using a two-stage thermal procedure involving hydrothermal treatment of glucose and dicyandiamide followed by high temperature

[a]*Department of Chemistry, American University, 4400 Massachusetts Avenue N.W., Washington, DC 20016, USA. E-mail: szou@american.edu*
[b]*Department of Chemistry and Biochemistry, University of California, 1156 High Street, Santa Cruz, California 95064, USA. E-mail: shaowei@ucsc.edu*

†Electronic supplementary information (ESI) available: Raman spectra, additional electrochemical data, and comparison of ORR performance with other N,Fe codoped carbons in the literature. See DOI: 10.1039/c6nr05884a

pyrolysis.[28] In another study,[29] nitrogen-doped porous graphene/carbon composites were fabricated by Men *et al.* using high temperature pyrolysis and KOH activation.

Herein, we report the synthesis of a new type of Fe and N-codoped ordered mesoporous carbon, which was formed by a cost-effective colloidal silica template method[16,30,31] using *o*-phenylenediamine (*o*PD), melamine and $FeCl_3{\cdot}6H_2O$ as the precursors. The obtained catalysts possessed a large specific surface area (up to 953.8 $cm^2\ g^{-1}$), uniform pore size (*ca.* 25 nm) and were highly doped with N (along with a trace amount of Fe). Electrochemical measurements showed that the ORR performance was even better than that of commercial Pt/C catalysts in alkaline media, within the context of onset potential, selectivity to form water, long-term stability, and tolerance against methanol crossover.

Experimental section

Chemicals

Melamine (99%), *o*-phenylenediamine (*o*PD), ammonium peroxydisulfate (APS, 98%), $FeCl_3{\cdot}6H_2O$ (≥98%), HCl (37%), HF (48%), colloidal silica (LUDOX TM-40, *ca.* 22 nm in dia., 40 wt% in water), Nafion solution (5 wt%) and commercial 20 wt% Pt/C catalysts were purchased from Sigma Aldrich and used without further purification. Water was supplied from a Barnstead Nanopure water purification system (18.3 MΩ·cm).

Sample preparation

The preparation of Fe and N codoped ordered mesoporous carbons is summarized in Scheme 1. In a typical experiment, 1.5 g of *o*PD, 6 g of melamine and 0.5 g of $FeCl_3{\cdot}6H_2O$ were dissolved in 100 mL of 0.5 M HCl. The mixture was stirred vigorously for 10 min, into which was then added 30 mL of a colloidal silica solution. 50 mL of a 1.0 M HCl solution containing 3.0 g APS was slowly added into the above mixture under vigorous stirring to initiate polymerization of *o*PD, as manifested by the appearance of a blood-red solution color. The mixture was stirred for another 24 h at 5 °C before being dried by rotary evaporation, and pyrolyzed under an argon gas flow at 900 °C in a tube furnace for 1 h at a ramp rate of 5 °C min^{-1}. The silica colloids were then removed by using a 24% HF solution, followed by centrifugation and washing with deionized water for several times to obtain Fe,N-codoped ordered mesoporous carbon, which was denoted as Fe,N-OMC.

Two control samples were prepared in a similar fashion but in the absence of either colloidal silica or $FeCl_3{\cdot}6H_2O$, and referred to as Fe,N-C and N-OMC, respectively.

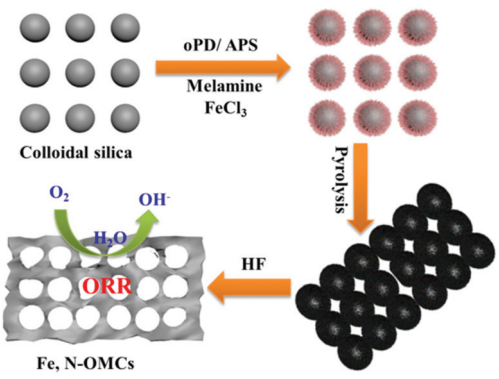

Scheme 1 Schematic of the synthetic procedure for ordered mesoporous carbon codoped with Fe and N.

Characterizations

The morphology of the obtained materials was examined by a high-resolution transmission electron microscope (HRTEM, JEOL JEM-2010). X-ray diffraction (XRD) patterns were recorded at room temperature using a Bruker D8 diffractometer with Cu K_α radiation (λ = 0.1541 nm). Raman spectra were collected using a confocal LabRAM HR800 spectrometer (Horiba JobinYvon, FR.) at an excitation wavelength of 514 nm from an argon ion laser. Nitrogen adsorption/desorption isotherms were recorded at 77 K using a Micromeritics ASAP 2020 instrument. X-ray photoelectron spectroscopy (XPS) measurements were conducted on a PHI X-tool instrument.

Electrochemistry

Electrochemical measurements were performed on an electrochemical workstation (CHI 760C, CH Instruments Inc.) with a three-electrode cell at room temperature. A platinum foil and a Ag/AgCl (saturated KCl) electrode were used as the counter and reference electrode, respectively. The working electrode was a rotating ring-disk electrode (RRDE) with a glassy carbon disk (GCE, 5.61 mm in diameter) and a Pt ring with a collection efficiency of 37% (Pine Instrument). To prepare the catalyst inks, 2 mg of the samples prepared above was added into 1 mL of a 4 : 1 (v : v) water/ethanol mixed solvent along with 20 μL of a Nafion solution (5%), and sonicated for 30 min. 10 μL of the inks was pipetted onto the clean GCE surface and dried at room temperature for 20 min at a catalyst loading of 0.08 mg cm^{-2}. For comparison, commercial Pt/C was loaded on the GCE surface using the same procedure (also at the loading of 0.08 mg cm^{-2}). ORR polarization curves were acquired in an O_2-saturated 0.1 M KOH aqueous solution at various rotation rates (225 to 2500 rpm).

In all measurements, the Ag/AgCl reference electrode was calibrated with respect to a reversible hydrogen electrode (RHE). The calibration was performed in 0.1 M KOH saturated with high-purity (99.999%) hydrogen gas with a Pt wire as the working electrode. Cyclic voltammograms were carried out at the scan rate of 1 mV s^{-1}, and the average of the two potentials at which the current crossed zero in both anodic and cathodic scans was taken as the thermodynamic potential of the RHE. In 0.1 M KOH, $E_{RHE} = E_{Ag/AgCl} + 0.966$ V. The geometrical area of the GCE was used to calculate the current density.

Results and discussion

In the present study, mesoporous carbon was prepared in a three-step procedure (Scheme 1): (a) polymerization of *o*PD on the colloidal silica surfaces initiated by APS, and entrapment of Fe ions and melamine which has been shown to increase nitrogen content in the final product;[32] (b) pyrolysis at elevated temperatures led to carbonization of the polymer layers to form mesh-like structures, which was facilitated by Fe ions;[33] and (c) removal of the colloidal silica templates by HF resulted in the formation of ordered mesoporous carbon. The structure and morphology of the obtained samples were first characterized by TEM measurements. One can see that in the absence of colloidal silica templates, the Fe,N-C sample exhibited a nonporous structure with a rather smooth surface morphology (Fig. 1a). In contrast, the incorporation of silica colloids (*ca.* 22 nm in dia.) as sacrificial templates produced a mesh-like structure with a number of uniform pores of around 25 nm, as manifested by both Fe,N-OMC (Fig. 1b) and N-OMC (Fig. 1c) samples. From the corresponding XRD patterns in Fig. 1d, two diffraction peaks can be identified at around 25.0° and 43.5°, which might be assigned to the (002) and (100) diffractions of hexagonal graphitic carbons, respectively.[34] Interestingly, the (002) diffraction can be found to shift to a lower angle from Fe, N-C (26.0°, black curve), to Fe,N-OMC (25.1°, red curve) and to N-OMC (24.5°, blue curve), indicating an increase of the interplanar distance.[35] This is consistent with results from Raman measurements, where Fe,N-C, Fe,N-OMC and N-OMC all showed a D band at 1344 cm^{-1} and a G band at 1605 cm^{-1}, and the ratio of the band intensities (I_D/I_G) increased in the order of Fe,N-C (1.01) < Fe,N-OMC (1.12) < N-OMC (1.15) (Fig. S1†). This confirmed the formation of hexagonal graphitic carbons, and the incorporation of silica colloid templates in the sample preparation indeed resulted in an increasing defective structure of the final carbon materials.

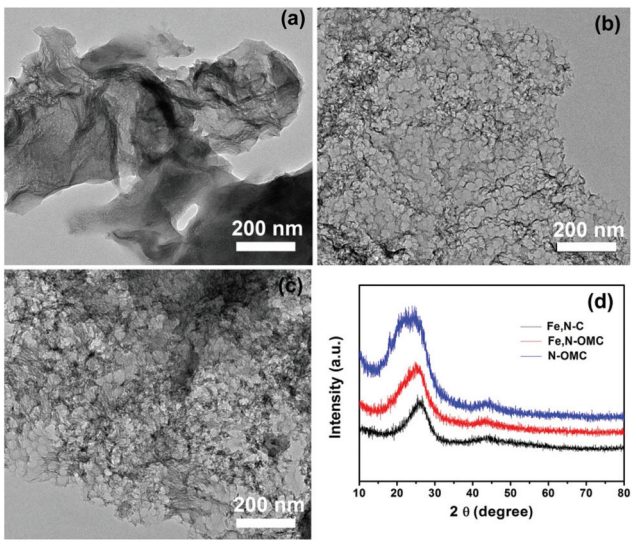

Fig. 1 Representative TEM images of (a) Fe,N-C, (b) Fe,N-OMC and (c) N-OMC; and (d) XRD patterns of the three samples.

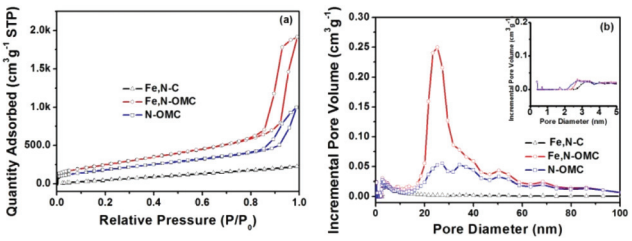

Fig. 2 (a) Nitrogen adsorption/desorption isotherms and (b) pore size distribution of Fe,N-C, Fe,N-OMC and N-OMC. Inset to panel (b) is the zoom-in of the pore-size distributions at pore diameters lower than 5 nm.

Fig. 2 depicts the N_2 adsorption/desorption isotherms and pore size distribution (PSD) of the three samples. From Fig. 2a, it can be seen that all samples showed a slow increase of adsorption at low relative pressures ($P/P_0 \leq 0.1$), indicating low concentrations of microporous structures in the materials. For both Fe,N-OMC (red curve) and N-OMC (blue curve), a type-IV adsorption/desorption isotherm was observed, which exhibited more abundant adsorption at higher relative pressures and a distinct hysteresis loop extended from P/P_0 = 0.85 to 1.0. This observation suggested the formation of a mesoporous structure in these two samples,[8,34] in contrast to Fe,N-C (black curve) where no hysteresis loop was observed as no silicon colloid templates were used. Consistent results were obtained in PSD analysis where the PSD was calculated using the Barrett–Joyner–Halenda (BJH) method. It can be seen from Fig. 2b that Fe,N-OMC and N-OMC exhibited a narrow PSD that was mainly centered at ~25 nm, rather comparable to the diameter of the colloidal silica templates (*ca.* 22 nm), in contrast to Fe,N-C where only a weak peak was located at 3.2 nm (inset to Fig. 2b). Table 1 summarized the Brunauer–Emmett–Teller (BET) surface area and total pore volume of Fe,N-C, Fe, N-OMC and N-OMC. The specific surface area was 953.8 m^2 g^{-1} for Fe,N-OMC and 698.2 m^2 g^{-1} for N-OMC, much higher than that of Fe,N-C (299.8 m^2 g^{-1}). These results show that colloidal silica may be used as sacrificial templates in the effective preparation of well controlled mesoporous carbon. Importantly, the Fe,N-OMC sample exhibited the highest surface area (953.8 m^2 g^{-1}) and biggest total pore volume of 2.96 cm^3 g^{-1} among the series of samples, with the pore size primarily in the range of 20 to 30 nm that is known to be optimal for mass transport of ORR species.[36,37]

Table 1 Summary of results obtained from nitrogen adsorption–desorption analysis

Sample	S_{BET} (m^2 g^{-1})	Pore volumes (cm^3 g^{-1})
Fe,N-C	299.8	0.35
Fe,N-OMC	953.8	2.96
N-OMC	698.2	1.55

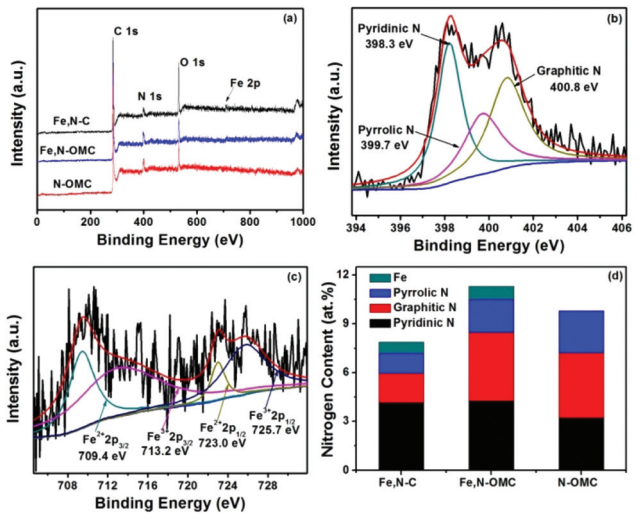

Fig. 3 (a) XPS survey spectra and high-resolution scans of (b) N1s and (c) Fe 2P of Fe,N-OMC. Black curves are experimental data and colored curves are deconvolution fits. (d) Nitrogen and iron contents in the Fe, N-C, Fe,N-OMC, and N-OMC.

XPS measurements were then carried out to examine the valence states and elemental compositions of the obtained samples. From the survey spectra in Fig. 3a, four predominant peaks can be readily identified at 284.6, 401.0, 532.0 and 711.0 eV, which may be assigned to the C 1s, N 1s, O 1s and Fe 2p electrons, respectively. Based on the integrated peak areas, the atomic concentrations of these elements were summarized in Table 2. It can be seen that the Fe,N-OMC sample exhibited the highest N concentrations at 10.5 at%, as compared to 9.8 at% for N-OMC and 7.2 at% for Fe,N-C, whereas the Fe content was drastically lower for both Fe,N-C (0.7 at%) and Fe,N-OMC (0.8 at%).

Furthermore, deconvolution of the high-resolution N 1s spectra (Fig. 3b and S2a, b†) yielded three peaks at 398.3, 399.7, and 400.8 eV, which were consistent with pyridinic, pyrrolic, and graphitic N, respectively, indicating that nitrogen was indeed embedded into the carbon skeletons. Based on the integrated peak areas, the fraction of each nitrogen components was quantified. As shown in Fig. 3d, the graphitic and pyridinic nitrogens were dominant in all three samples. The concentration of graphitic N decreased in the order of Fe, N-OMC (4.2 at%) > N-OMC (4.0 at%) > Fe,N-C (1.8 at%). The concentration of pyridinic N in Fe,N-OMC (4.3 at%) was also higher than those in Fe,N-C (4.1 at%) and N-OMC (3.2 at%). Note that graphitic N and pyridinic N have both been proposed as the dopants that are responsible for the formation of ORR active sites.[38–40] Thus a high concentration of these dopants may lead to a high ORR performance. Furthermore, Fig. 3c and S2c† showed the high-resolution scan of the Fe 2p electrons, where deconvolution yielded two pairs of peaks for Fe^{2+} (709.4 and 723.0 eV) and Fe^{3+} (713.2 and 725.7 eV), suggesting the entrapment of iron nitrides (Fe-N_x) and iron oxides in the porous carbon.[41,42] Yet, as mentioned above, the total Fe content was very low, only at 0.7 at% for Fe,N-C and 0.8 at% for Fe,N-OMC (Fig. 3d).

Significantly, the doped carbons all exhibited apparent electrocatalytic activity towards ORR. Fig. 4a showed the CVs of a GCE modified with Fe,N-C, Fe,N-OMC, or N-OMC in a 0.1 M

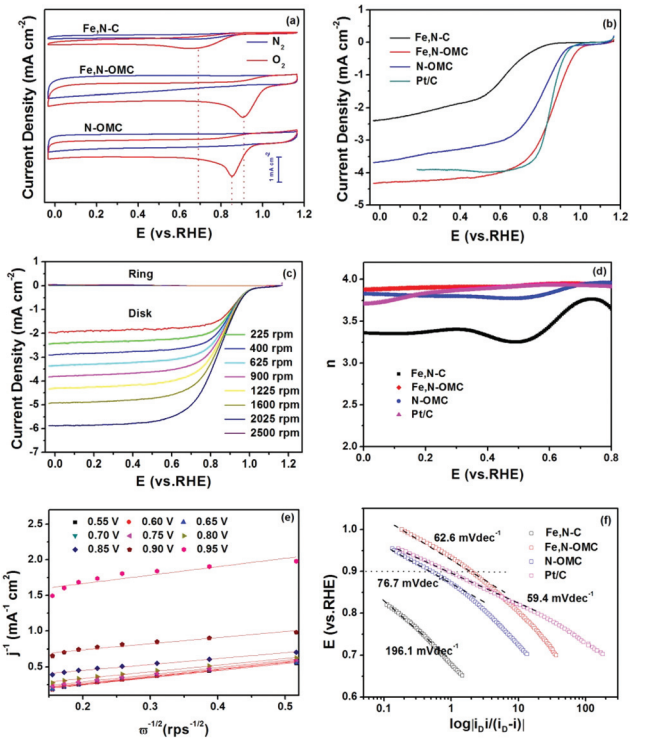

Fig. 4 (a) Cyclic voltammograms of Fe,N-C, Fe,N-OMC and N-OMC in N_2 and O_2-saturated 0.1 M KOH; scan rate 10 mV s^{-1}. (b) Linear sweep voltammograms of Fe,N-Cs, Fe,N-OMC, N-OMC and Pt/C at the electrode rotation rate of 1600 rpm and potential scan rate of 10 mV s^{-1}; (c) Polarization curves for ORR on Fe,N-OMC electrode in O_2-saturated 0.1 M KOH solution at various rotation rates, with the ring potential set at +1.47 V *vs.* RHE; (d) Variation of the number of electron transfer (*n*) with electrode potential for Fe,N-Cs, Fe,N-OMC, N-OMC and Pt/C; (e) Koutecky–Levich plots of Fe,N-OMC at different electrode potentials; (f) Tafel plots of Fe,N-Cs, Fe,N-OMC, N-OMC and Pt/C.

Table 2 Elemental contents and concentrations of N species in carbon catalysts determined by XPS measurements

Sample	C (at%)	O (at%)	Fe (at%)	N (at%)	Pyrinidic N	Pyrrolic N	Graphitic N
Fe,N-C	74.2	17.9	0.7	7.2	4.15	1.24	1.81
Fe,N-OMC	77.9	10.8	0.8	10.5	4.27	2.03	4.20
N-OMC	82.2	8.0	0	9.8	3.23	2.58	3.99

KOH solution saturated with N_2 or O_2 at the potential scan rate of 10 mV s^{-1}. In the N_2-saturated 0.1 M KOH solution, only featureless double layer charging was observed. When the solution was saturated with O_2, all three samples exhibited a well-defined cathodic reduction peaks, with the peak potential at +0.69 V for Fe,N-C, +0.91 V for Fe,N-OMC, and +0.85 V for N-OMC, indicating effective electrochemical reduction of oxygen on the three samples and Fe,N-OMC appeared to stand out as the best catalyst among the three catalysts.

To further compare the ORR activity, RDE voltammograms were acquired at the rotation rate of 1600 rpm in O_2 saturated 0.1 M KOH. For comparison, results from a commercial Pt/C catalyst were also included. From Fig. 4b, it can be seen that the onset potential of Fe,N-OMC for ORR was +0.99 V, more positive than those of Fe,N-C (+0.76 V), N-OMC (+0.92 V) and Pt/C (+0.96 V). These results were in agreement with the CV observations in Fig. 4a. In addition, the diffusion-limited current density of Fe,N-OMC was also higher than those of Fe, N-C, and N-OMC, and comparable to that of Pt/C. For instance, the current density at +0.40 V decreased in the order of 4.16 mA cm^{-2} (Fe,N-OMC) > 3.92 mA cm^{-2} (Pt/C) > 3.27 mA cm^{-2} (N-OMC) > 1.87 mA cm^{-2} (Fe,N-C).

This remarkable performance may be attributed to several factors. First, the concentration of graphitic and pyridinic N, which play a predominant role in determining the electrochemical activity of carbon catalysts for ORR,[5] is higher in Fe, N-OMC than in Fe,N-C and N-OMC, Both graphitic and pyridinic N have been shown to facilitate O_2 adsorption and the rate-limiting step of first electron transfer in ORR.[43,44] Second, the covalent integration of Fe-N_x sites into π-conjugated carbon basal planes modified the electron donating/withdrawing capability of the carbonaceous ligand, thus improving the ORR activity.[45–47] Third, the Fe,N-OMC possess a relatively larger specific surface area and a unique pore structure which are expected to maximize the number of accessible active sites as well as to facilitate the reactant transport inside this material. Significantly, the ORR activity of Fe,N-OMC was at least comparable to, if not higher than, the leading results reported in recent literatures where Fe and N codoped carbon materials were prepared by different approaches (Table S1†).[16,22,42,45,46,48–52]

We also performed RRDE measurements at various rotation rates (Fig. 4c and S3a–c†). It can be seen from the voltammetric profiles of Fe,N-OMC that the disk current density increased with increasing rotation rate (from 225 to 2500 rpm); and the ring currents were at least an order of magnitude lower, indicating a low concentration of peroxide species produced during ORR at the disk electrode.[53] The number of electron transfer (n) at different potentials were calculated by eqn (1),[6]

$$n = \frac{4I_D}{I_D + I_R/N} \quad (1)$$

where I_D represents the disk current, I_R is the ring current, and N is the RRDE collection efficiency (37%). Fig. 4d displays the variation of n with electrode potential for the three carbon catalysts. The average n values were estimated to be 3.4 for Fe, N-C, 3.9 for Fe,N-OMC, 3.8 for N-OMC, and 3.9 for Pt/C within the electrode potential range of 0 to +0.90 V. These results suggested that at Fe,N-OMC, N-OMC and Pt/C, ORR occurred largely *via* the four-electron pathway. The corresponding Koutecky–Levich (K–L) plots (j^{-1} *vs.* $\omega^{1/2}$) were depicted in Fig. 4e and S3d–f† from the RRDE voltammograms in Fig. 4c and S3a–c† by using eqn (2) and (3),

$$\frac{1}{j} = \frac{1}{j_K} + \frac{1}{j_D} = \frac{1}{j_K} + \frac{1}{B\omega^{1/2}} \quad (2)$$

$$B = 0.62nFD^{2/3}\nu^{-1/6}C_{O_2} \quad (3)$$

where j, j_K, and j_D are the measured, kinetic, and diffusion limited current densities respectively, ω is the angular velocity of the electrode, n is the number of electron transfer involved in the oxygen reduction reaction, F is the Faraday constant (96 485 C mol^{-1}), D is the oxygen diffusion coefficient (1.9×10^{-5} cm^2 s^{-1}), ν is the kinematic viscosity of the electrolyte solution (0.01 cm^2 s^{-1}) and C_{O_2} is the bulk concentration of oxygen (1.2×10^{-3} mol L^{-1}).[54] It can be seen that the K–L plots display good linearity at different potentials for the Fe, N-C, Fe,N-OMC, N-OMC and Pt/C catalysts, indicating first-order reaction kinetics for ORR with respect to the concentration of dissolved oxygen. The corresponding Tafel slopes were also estimated at 196.1 mV dec^{-1} for Fe,N-C, 62.6 mV dec^{-1} for Fe,N-OMC, 76.7 mV dec^{-1} for N-OMC and 59.4 mV dec^{-1} for Pt/C (Fig. 4f). That is, the Tafel slopes for Fe,N-OMC and N-OMC are actually close to that of commercial Pt/C, suggesting a similar ORR mechanism among these three catalysts and the rate-determining step for ORR was the first electron reduction of molecular oxygen.[55,56] However, the activity was clearly different. For instance, the kinetic current density at +0.90 V was 1.98 mA cm^{-2} for Fe,N-OMC, markedly higher than 0.92 mA cm^{-2} for Pt/C, 0.52 mA cm^{-2} for N-OMC, and nearly zero for Fe,N-C. The remarkable ORR performance of Fe,N-OMC may be ascribed to the co-doping with Fe and N and the formation of a mesoporous structure.

From Table 2, one can see that whereas the concentration of N dopants was very close between Fe,N-OMC and N-OMC (so were the fractions of the pyridinic and graphitic nitrogens), the ORR activity was about 4 times more active with the former than with the latter, whereas the BET specific surface area was only about 40% larger for the former (Table 1). This suggests that the primary contributions to the marked difference of the ORR activity most likely arose from the Fe dopants. In other words, both N and Fe dopants are responsible for the ORR activity.[7,56] In addition, one can see that the concentrations of Fe and N dopants in Fe,N-OMC were very close to those in Fe, N-C. However, there is a vast disparity of the specific activity between these two samples. This may be correlated to the BET specific surface area of Fe,N-OMC that was more than three times that of Fe,N-C (along with a pore volume that was almost 10 times larger, Table 1). This indicates the significance of the formation of a mesoporous structure in facilitating oxygen reduction. Taken together, these results suggest that both

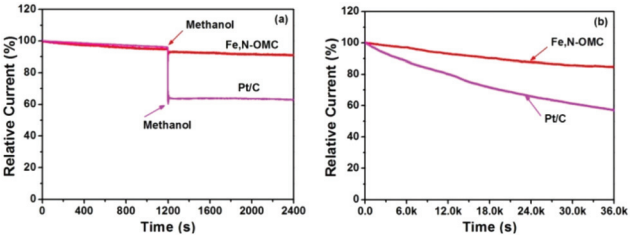

Fig. 5 (a) Current–time (*i*–*t*) responses for ORR on Fe,N-OMC and Pt/C modified electrodes at reduction peak potential (+0.91 V *vs.* RHE) in an O_2-saturated 0.1 M KOH solution with the addition of 3 M methanol at 1200 s, which is marked with an arrow. (b) Chronoamperometric profiles of Fe,N-OMC and Pt/C electrodes for 36 000 s in O_2-saturated 0.1 M KOH at +0.91 V *vs.* RHE at a rotation speed of 900 rpm.

Fe and N doping is critical in activating carbons for ORR, which is further facilitated by the formation of a mesoporous structure.

In addition, the tolerance to methanol crossover and stability for Fe,N-OMC and commercial Pt/C were evaluated and compared by chronoamperometric measurements where the potential was set at +0.91 V and at the rotation speed of 900 rpm in O_2-saturated 0.1 M KOH. As shown in Fig. 5a, when 3 M methanol was injected at 1200 s to the solution, the current density of Pt/C showed a sharp drop of about 40%, whereas the voltammetric profiles for Fe,N-OMC remained almost invariant. These results indicate that Fe,N-OMC was not vulnerable to methanol crossover. The Fe,N-OMC sample also exhibited remarkable long-term stability. As depicted in Fig. 5b, after continuous operation for 36 000 s the ORR activity only lost about 14% on Fe,N-OMC, in comparison to a 43% loss at commercial Pt/C. These results suggested that the Fe,N-OMC catalyst possessed significantly better stability than commercial Pt/C.

Conclusions

In this study, Fe and N codoped ordered mesoporous carbons with a large surface area and uniform pores were prepared *via* a simple colloidal silica template method. The samples were thoroughly characterized by TEM, Raman, nitrogen adsorption, XRD, and XPS measurements. The Fe,N-OMC sample stood out as the best ORR catalysts among the series, most probably due to a high specific surface area, ordered mesoporous structure and high concentration of pyridinic N, graphitic N, and iron dopants. Significantly, the ORR performance was highly comparable to that of commercial Pt/C (20 wt%) catalysts, along with enhanced long-term stability and methanol tolerance. The results from this study provide a new approach to the preparation of non-precious metal catalysts with a high density of accessible active sites that may rival Pt-based catalysts in fuel cell electrocatalysis.

Acknowledgements

This work was partially supported by the National Science Foundation (CHE-1265635 and DMR-1409396 to SWC and CHE-1559670 to SZ).

References

1 M. K. Debe, *Nature*, 2012, **486**, 43–51.
2 K. Gong, F. Du, Z. Xia, M. Durstock and L. Dai, *Science*, 2009, **323**, 760–764.
3 C. V. Rao, C. R. Cabrera and Y. Ishikawa, *J. Phys. Chem. Lett.*, 2010, **1**, 2622–2627.
4 T. Sharifi, G. Hu, X. Jia and T. Wågberg, *ACS Nano*, 2012, **6**, 8904–8912.
5 D. Geng, Y. Chen, Y. Chen, Y. Li, R. Li, X. Sun, S. Ye and S. Knights, *Energy Environ. Sci.*, 2011, **4**, 760–764.
6 K. Parvez, S. Yang, Y. Hernandez, A. Winter, A. Turchanin, X. Feng and K. Müllen, *ACS Nano*, 2012, **6**, 9541–9550.
7 L. Lai, J. R. Potts, D. Zhan, L. Wang, C. K. Poh, C. Tang, H. Gong, Z. Shen, J. Lin and R. S. Ruoff, *Energy Environ. Sci.*, 2012, **5**, 7936–7942.
8 H.-W. Liang, X. Zhuang, S. Brüller, X. Feng and K. Müllen, *Nat. Commun.*, 2014, **5**.
9 J. Liang, X. Du, C. Gibson, X. W. Du and S. Z. Qiao, *Adv. Mater.*, 2013, **25**, 6226–6231.
10 R. Liu, D. Wu, X. Feng and K. Müllen, *Angew. Chem., Int. Ed.*, 2010, **122**, 2619–2623.
11 W. Niu, L. Li, J. Liu, N. Wang, W. Li, Z. Tang, W. Zhou and S. Chen, *Small*, 2016, **12**, 1900–1908.
12 X. Liu, Y. Zhou, W. Zhou, L. Li, S. Huang and S. Chen, *Nanoscale*, 2015, **7**, 6136–6142.
13 D.-W. Wang and D. Su, *Energy Environ. Sci.*, 2014, **7**, 576–591.
14 Y. Nie, L. Li and Z. Wei, *Chem. Soc. Rev.*, 2015, **44**, 2168–2201.
15 M. Lefèvre, E. Proietti, F. Jaouen and J.-P. Dodelet, *Science*, 2009, **324**, 71–74.
16 H.-W. Liang, W. Wei, Z.-S. Wu, X. Feng and K. Müllen, *J. Am. Chem. Soc.*, 2013, **135**, 16002–16005.
17 H. Peng, F. Liu, X. Liu, S. Liao, C. You, X. Tian, H. Nan, F. Luo, H. Song, Z. Fu and P. Huang, *ACS Catal.*, 2014, **4**, 3797–3805.
18 S. Wang, M. Zhu, X. Bao, J. Wang, C. Chen, H. Li and Y. Wang, *ChemCatChem*, 2015, **7**, 2937–2944.
19 H. Jiang, Y. Yao, Y. Zhu, Y. Liu, Y. Su, X. Yang and C. Li, *ACS Appl. Mater. Interfaces*, 2015, **7**, 21511–21520.
20 G. Wu, K. L. More, C. M. Johnston and P. Zelenay, *Science*, 2011, **332**, 443–447.
21 J. Masa, A. Zhao, W. Xia, Z. Sun, B. Mei, M. Muhler and W. Schuhmann, *Electrochem. Commun.*, 2013, **34**, 113–116.
22 J. Liu, X. Sun, P. Song, Y. Zhang, W. Xing and W. Xu, *Adv. Mater.*, 2013, **25**, 6879–6883.
23 D. Shin, B. Jeong, B. S. Mun, H. Jeon, H.-J. Shin, J. Baik and J. Lee, *J. Phys. Chem. C*, 2013, **117**, 11619–11624.

24 S. Maldonado and K. J. Stevenson, *J. Phys. Chem. B*, 2004, **108**, 11375–11383.
25 N. Ranjbar Sahraie, J. P. Paraknowitsch, C. Göbel, A. Thomas and P. Strasser, *J. Am. Chem. Soc.*, 2014, **136**, 14486–14497.
26 W. Yang, T.-P. Fellinger and M. Antonietti, *J. Am. Chem. Soc.*, 2011, **133**, 206–209.
27 W. He, C. Jiang, J. Wang and L. Lu, *Angew. Chem., Int. Ed.*, 2014, **53**, 9503–9507.
28 X. Liu, L. Li, W. Zhou, Y. Zhou, W. Niu and S. Chen, *ChemElectroChem*, 2015, **2**, 803–810.
29 B. Men, Y. Sun, M. Li, C. Hu, M. Zhang, L. Wang, Y. Tang, Y. Chen, P. Wan and J. Pan, *ACS Appl. Mater. Interfaces*, 2016, **8**, 1415–1423.
30 J. Liang, Y. Jiao, M. Jaroniec and S. Z. Qiao, *Angew. Chem., Int. Ed.*, 2012, **51**, 11496–11500.
31 W. Wei, H. Liang, K. Parvez, X. Zhuang, X. Feng and K. Müllen, *Angew. Chem., Int. Ed.*, 2014, **126**, 1596–1600.
32 S. Zhang, H. Zhang, Q. Liu and S. Chen, *J. Mater. Chem. A*, 2013, **1**, 3302–3308.
33 H. Peng, S. Hou, D. Dang, B. Zhang, F. Liu, R. Zheng, F. Luo, H. Song, P. Huang and S. Liao, *Appl. Catal., B*, 2014, **158–159**, 60–69.
34 L. Qie, W. M. Chen, Z. H. Wang, Q. G. Shao, X. Li, L. X. Yuan, X. L. Hu, W. X. Zhang and Y. H. Huang, *Adv. Mater.*, 2012, **24**, 2047–2050.
35 F. Su, C. K. Poh, J. S. Chen, G. Xu, D. Wang, Q. Li, J. Lin and X. W. Lou, *Energy Environ. Sci.*, 2011, **4**, 717–724.
36 J. Liang, R. F. Zhou, X. M. Chen, Y. H. Tang and S. Z. Qiao, *Adv. Mater.*, 2014, **26**, 6074–6079.
37 Z. Li, G. Li, L. Jiang, J. Li, G. Sun, C. Xia and F. Li, *Angew. Chem., Int. Ed.*, 2015, **54**, 1494–1498.
38 W. Ding, Z. Wei, S. Chen, X. Qi, T. Yang, J. Hu, D. Wang, L.-J. Wan, S. F. Alvi and L. Li, *Angew. Chem., Int. Ed.*, 2013, **52**, 11755–11759.
39 D. H. Guo, R. Shibuya, C. Akiba, S. Saji, T. Kondo and J. Nakamura, *Science*, 2016, **351**, 361–365.
40 B. Men, Y. Sun, M. Li, C. Hu, M. Zhang, L. Wang, Y. Tang, Y. Chen, P. Wan and J. Pan, *ACS Appl. Mater. Interfaces*, 2016, **8**, 1415–1423.
41 A. Velázquez-Palenzuela, L. Zhang, L. Wang, P. L. Cabot, E. Brillas, K. Tsay and J. Zhang, *J. Phys. Chem. C*, 2011, **115**, 12929–12940.
42 X. Cui, S. Yang, X. Yan, J. Leng, S. Shuang, P. M. Ajayan and Z. Zhang, *Adv. Funct. Mater.*, 2016, **26**, 5708–5717.
43 H. Kim, K. Lee, S. I. Woo and Y. Jung, *Phys. Chem. Chem. Phys.*, 2011, **13**, 17505–17510.
44 D. Deng, X. Pan, L. Yu, Y. Cui, Y. Jiang, J. Qi, W.-X. Li, Q. Fu, X. Ma, Q. Xue, G. Sun and X. Bao, *Chem. Mater.*, 2011, **23**, 1188–1193.
45 L. Lin, Q. Zhu and A.-W. Xu, *J. Am. Chem. Soc.*, 2014, **136**, 11027–11033.
46 G. A. Ferrero, K. Preuss, A. Marinovic, A. B. Jorge, N. Mansor, D. J. L. Brett, A. B. Fuertes, M. Sevilla and M.-M. Titirici, *ACS Nano*, 2016, **10**, 5922–5932.
47 V. A. Setyowati, H.-C. Huang, C.-C. Liu and C.-H. Wang, *Electrochim. Acta*, 2016, **211**, 933–940.
48 R. Silva, D. Voiry, M. Chhowalla and T. Asefa, *J. Am. Chem. Soc.*, 2013, **135**, 7823–7826.
49 Y. Hou, T. Huang, Z. Wen, S. Mao, S. Cui and J. Chen, *Adv. Energy Mater.*, 2014, **4**, 1400337.
50 J. Xi, Y. Xia, Y. Xu, J. Xiao and S. Wang, *Chem. Commun.*, 2015, **51**, 10479–10482.
51 X.-H. Yan and B.-Q. Xu, *J. Mater. Chem. A*, 2014, **2**, 8617–8622.
52 F.-L. Meng, Z.-L. Wang, H.-X. Zhong, J. Wang, J.-M. Yan and X.-B. Zhang, *Adv. Mater.*, 2016, **28**, 7948–7955.
53 Z. Y. Wu, X. X. Xu, B. C. Hu, H. W. Liang, Y. Lin, L. F. Chen and S. H. Yu, *Angew. Chem., Int. Ed.*, 2015, **54**, 8179–8183.
54 R. E. Davis, G. L. Horvath and C. W. Tobias, *Electrochim. Acta*, 1967, **12**, 287–297.
55 M. Xiao, J. Zhu, L. Feng, C. Liu and W. Xing, *Adv. Mater.*, 2015, **27**, 2521–2527.
56 W. Niu, L. Li, X. Liu, N. Wang, J. Liu, W. Zhou, Z. Tang and S. Chen, *J. Am. Chem. Soc.*, 2015, **137**, 5555–5562.